



Bismuth vacancy mediated single unit cell Bi₂WO₆ nanosheets for boosting photocatalytic oxygen evolution

Jun Di^{a,b,1}, Chao Chen^{b,1}, Chao Zhu^b, Mengxia Ji^a, Jiexiang Xia^{a,c,**}, Cheng Yan^b, Wei Hao^b, Shuzhou Li^b, Huaming Li^{a,*}, Zheng Liu^{b,*}

^a School of Chemistry and Chemical Engineering, Institute for Energy Research, Jiangsu University, 301 Xuefu Road, Zhenjiang, 212013, PR China

^b Center for Programmable Materials, School of Materials Science & Engineering, Nanyang Technological University, Singapore, 639798, Singapore

^c Chemical Sciences Division, Oak Ridge National Laboratory, Oak Ridge, 37830, United States

ARTICLE INFO

Keywords:

Ultrathin Bi₂WO₆
Bismuth vacancies
Electronic structure
Photocatalytic
Oxygen evolution

ABSTRACT

Surface defects are critically important for photocatalytic reactions. Compared with the widely studied oxygen vacancies, engineering metal vacancies into photocatalysts and study the effect of metal vacancies on the photocatalytic performance is seldom reported. Herein, we engineering bismuth vacancies into Bi₂WO₆ via a template-directed strategy to form single unit cell ultrathin nanosheets. Aberration-corrected scanning transmission electron microscopy reveals the formation of bismuth vacancies in the Bi₂WO₆ ultrathin nanosheets. Density functional theory calculations suggest that the presence of bismuth vacancies create a new defect level in forbidden band and increased density of states at the valence band maximum, resulting in increased charge carrier concentration and electronic conductivity. Moreover, the bismuth vacancy structure benefit for the surface adsorption and activation of water molecule, which favors the water oxidation reactions. As a result, the prepared bismuth vacancy-rich Bi₂WO₆ exhibit significantly increased visible light photocatalytic oxygen evolution activity than the corresponding bulk Bi₂WO₆, which is the more challenging half-reaction for fuel-forming due to the sluggish reaction kinetics. This work open the door for designing other metal vacancies engineered photocatalysts via ultrathin-control strategy and achieving highly efficient photocatalytic performances.

1. Introduction

Photocatalytic solar energy conversion such as water splitting and CO₂ reduction has been regarded as effective approach to address the increasingly energy shortage and environmental pollution issues [1–5]. Only suitable semiconductor was required to convert sustainable solar energy to hydrocarbon fuels enable it rather promising. However, the oxidation reaction that can balance these fuel-forming reduction half reactions is the generation of oxygen, in which the sluggish kinetics feature of oxygen evolution process greatly limited the overall solar energy conversion efficiency [6]. Therefore, it is highly desirable and urgent to promote the water oxidation oxygen evolution activity.

As an Aurivillius phase oxide, bismuth tungstate (Bi₂WO₆) has been widely studied in photocatalysis field recent years due to its features of suitable band gap, nontoxicity, high stability and outstanding photocatalytic activity [7–9]. It belongs to the layered multicomponent metal

oxide, which crystallize in interlacing [Bi₂O₂]²⁺ slabs with [WO₄]²⁻ slabs with oxygen atoms shared between slabs to form chemical bonded [Bi₂O₂]²⁺-[WO₄]²⁻ stacks. Up to now, it has been employed for different photocatalytic applications such as hydrogen evolution [10], CO₂ reduction [11], selective organic synthesis [12] and pollutant removal [13]. Studies demonstrated that the Bi₂WO₆ materials with different architectures can display superior activity towards different photocatalytic applications. Therefore, it is hopeful to achieve the high-efficiency water oxidation behavior if reasonable design was performed to tune Bi₂WO₆ materials. In order to promote the photocatalytic performance to meet the potential industrialization requirement, several strategies have been proposed, in which engineering defects into the photocatalysts may be an effective strategy.

Studies have demonstrated abundant examples of the positive effect of surface defects on the enhancement of photocatalysis [14–17]. Even infinitesimal amount of surface defects could unlock the huge potential

* Corresponding authors.

** Corresponding author at: School of Chemistry and Chemical Engineering, Institute for Energy Research, Jiangsu University, 301 Xuefu Road, Zhenjiang, 212013, PR China.

E-mail addresses: xjx@ujs.edu.cn (J. Xia), lhm@ujs.edu.cn (H. Li), z.liu@ntu.edu.sg (Z. Liu).

¹ These authors contributed equally to this work.

that exists for tuning the energy band structure, carrier concentration, spin nature and so on, which following adjust the intrinsic properties [18]. Generally, the primary role of surface defects are concentrate on three aspects: (1) provide extra active sites and directly involved in the interfacial reactions, (2) tune the electronic structure to promote conductivity, (3) serve as centers for capturing photogenerated electrons and improves the charge separation efficiency. Up to now, the widely studied surface defects mainly center on oxygen vacancies, engineering metal vacancies into photocatalysts and study the effect of metal vacancies on the photocatalytic performance is seldom reported, owing to it is quite difficult to engineer and manipulate metal vacancies in a stable and reliable way [19]. Therefore, it is desirable to engineering metal vacancies into Bi_2WO_6 photocatalysts and explore the photocatalytic performance [8].

Considering the layered structure of Bi_2WO_6 , controlling the thickness to atomically-thin may be a feasible strategy to engineering surface defects into Bi_2WO_6 . When the thickness of materials is reduced to the atomic scale, their atomic-escape energy will become relatively small, many surface atoms can be more easily escape from the 2D lattice to form vacancies [18,20]. Herein, bismuth vacancies (V_{Bi}) are engineered into Bi_2WO_6 via a template-directed strategy to form single unit cell ultrathin nanosheets. By employing the beforehand prepared atomically-thick BiOBr nanosheets as precursors (the characterizations of atomically-thick BiOBr nanosheets were shown in Fig. S1), the Bi_2WO_6 ultrathin nanosheets can be achieved via the ion exchange process (Scheme S1). Since the BiOBr is a layered material with interlayer weak van der Waals forces, the Br^- layer are prone to be substituted by $[\text{WO}_4]^{2-}$ to form chemical bonded $[\text{Bi}_2\text{O}_2]^{2+} \cdot [\text{WO}_4]^{2-}$ stacks. The photocatalytic performance of the obtained V_{Bi} -rich Bi_2WO_6 was evaluated by the photocatalytic water oxidation reaction under visible light irradiation. Through multiple characterizations to determine the morphology, surface feature, and electronic structure, the relationship between the bismuth vacancies and the photocatalytic behavior was discussed in details.

2. Experimental

2.1. Synthesis of BiOBr ultrathin nanosheets

0.5 mmol $\text{Bi}(\text{NO}_3)_3 \cdot 5\text{H}_2\text{O}$ and 0.2 g PVP was initially dissolved in 15 mL 0.1 M mannitol solution under magnetic stirring at room temperature. Then, 5 mL KBr solution (0.1 M) was injected into the above solution under stirring. After being stirred for 30 min, the suspension was transfer to 25 mL Teflon-lined autoclave and subsequently heated at 160 °C for 3 h to achieve the BiOBr ultrathin nanosheets.

2.2. Synthesis of V_{Bi} -rich Bi_2WO_6

0.5 mmol BiOBr ultrathin nanosheets was dispersed in 20 mL water under ultrasound. Then 1 mmol Na_2WO_4 was added into above dispersions and stirring for 30 min. Subsequently, the above suspension was added into 25 mL Teflon-lined autoclave and heated at 140 °C for 1 h. After cooling down to room temperature, the precipitate was collected and washed with deionized water and ethanol for several times.

2.3. Synthesis of bulk Bi_2WO_6

2 mmol WO_3 and 2 mmol Bi_2O_3 was mixed in 20 mL ethanol at room temperature. After drying at 80 °C, the sample was calcined at 800 °C for 10 h in muffle furnace to obtain the bulk Bi_2WO_6 .

2.4. Characterization

The phase structure of as-synthesized Bi_2WO_6 ultrathin nanosheets was characterized by X-ray diffraction (XRD) using monochromatic $\text{Cu K}\alpha$ radiation (Shimadzu XRD-6000 diffractometer). The morphology

and structure were determined by transmission electron microscopy (TEM, JEOL JEM-2100F). Aberration-corrected scanning transmission electron microscopy at high-angular annular dark field (STEM-HAADF) images were recorded via a JEM-ARM200F operated at 80 kV. The composition and surface properties of the obtained samples were determined by X-ray photoelectron spectroscopy (XPS, VG MultiLab 2000 system). BET specific surface areas were characterized with the adsorption-desorption isotherms on the Micromeritics 3020 system. UV-vis diffuse reflectance spectra (DRS) was employed to study the optical properties of the obtained Bi_2WO_6 materials by using a UV-vis spectrophotometer (Shimadzu UV-2450). The electron spin resonance (ESR) signals of spin-trapped oxidative radicals were obtained on a Bruker model ESR JES-FA200 spectrometer using spin-trap reagent DMPO (Sigma Chemical Co.).

2.5. DFT calculation details

The first-principles simulations were conducted using the Vienna ab initio simulation package (VASP) [21], the projector augmented wave (PAW) potentials are used as pseudopotentials to describe the interactions between valence electrons and ions. The Perdew–Burke–Ernzerhof (PBE) functional of generalized gradient approximation (GGA) was used to describe the exchange-correlation of valence electrons [22]. For density of states, two modes were calculated: bulk and layer slab. The plane wave cutoff energy as set to be 500 eV, and the k-point mesh was set as a $6 \times 6 \times 2$ for bulk and $6 \times 6 \times 1$ for layer slab. The convergence criteria were 10^{-6} eV in electric relaxation energy and 10^{-5} eV in ionic relaxation energy. The optimized lattice constant for bulk Bi_2WO_6 was $5.536 \text{ \AA} \times 5.557 \text{ \AA} \times 16.783 \text{ \AA}$. In layer slab calculation, a 20 Å vacuum layer was added to avoid inter-layer interactions. For the simulation of defect layer slab, a $2 \times 2 \times 1$ supercell was established, and one Bi atoms was removed from each supercell, and the k-point mesh was reset to $4 \times 4 \times 1$, with all the other parameters remained unchanged.

2.6. Photocatalytic water oxidation

Photocatalytic water oxidation experiments were performed on Labsolar-IIIAG system (PerfectLight) using a 300 W Xe arc lamp with a 420 nm cutoff filter as the visible light source. 50 mg samples was dispersed in 50 mL H_2O and AgNO_3 (0.05 mol/L) was used as an electron sacrificial agent. The Ar evacuation was performed for at least 0.5 h to completely remove Air. The photocatalytic water oxidation reaction was typically carried out for 3 h and the generated O_2 amount was determined using an online gas chromatograph (Shimadzu GC-2010, TCD detector, Ar carrier).

3. Results and discussion

The crystal structure of the products after ion exchange process was determined by X-ray power diffraction. As shown in Fig. 1a, the peaks located at 2θ values of 28.4°, 32.8°, 47.1°, 55.8°, 58.6°, 68.6°, 76.1°, 78.3° can be indexed to (113), (006)/(200), (206)/(026), (119)/(208), (226), (400), (333), (420) crystal planes of orthorhombic Bi_2WO_6 (JCPDS card No. 73-2020), respectively. The weak and broad diffraction peaks showed that the obtained products were nanoscale structure. To determine the morphology and surface microstructure of the as-prepared Bi_2WO_6 sample, transmission electron microscopy (TEM) was carried out. The TEM image in Fig. 1b clearly showed their sheet-like morphology, with the average size about 50*50 nm. The nearly transparent feature of the nanosheets suggesting the ultrathin thickness of the as-obtained Bi_2WO_6 nanosheets (Fig. 1c). The lattice spacing can be determined to be 0.273 and 0.272 nm, corresponding to the (200) and (020) planes of Bi_2WO_6 , suggesting the (001) orientation exposure of Bi_2WO_6 nanosheets (Fig. 1d). To further determine the thickness of the Bi_2WO_6 nanosheets, atomic force microscopic was carried out and the result was shown in Fig. S2. The Bi_2WO_6 nanosheets displayed uniform

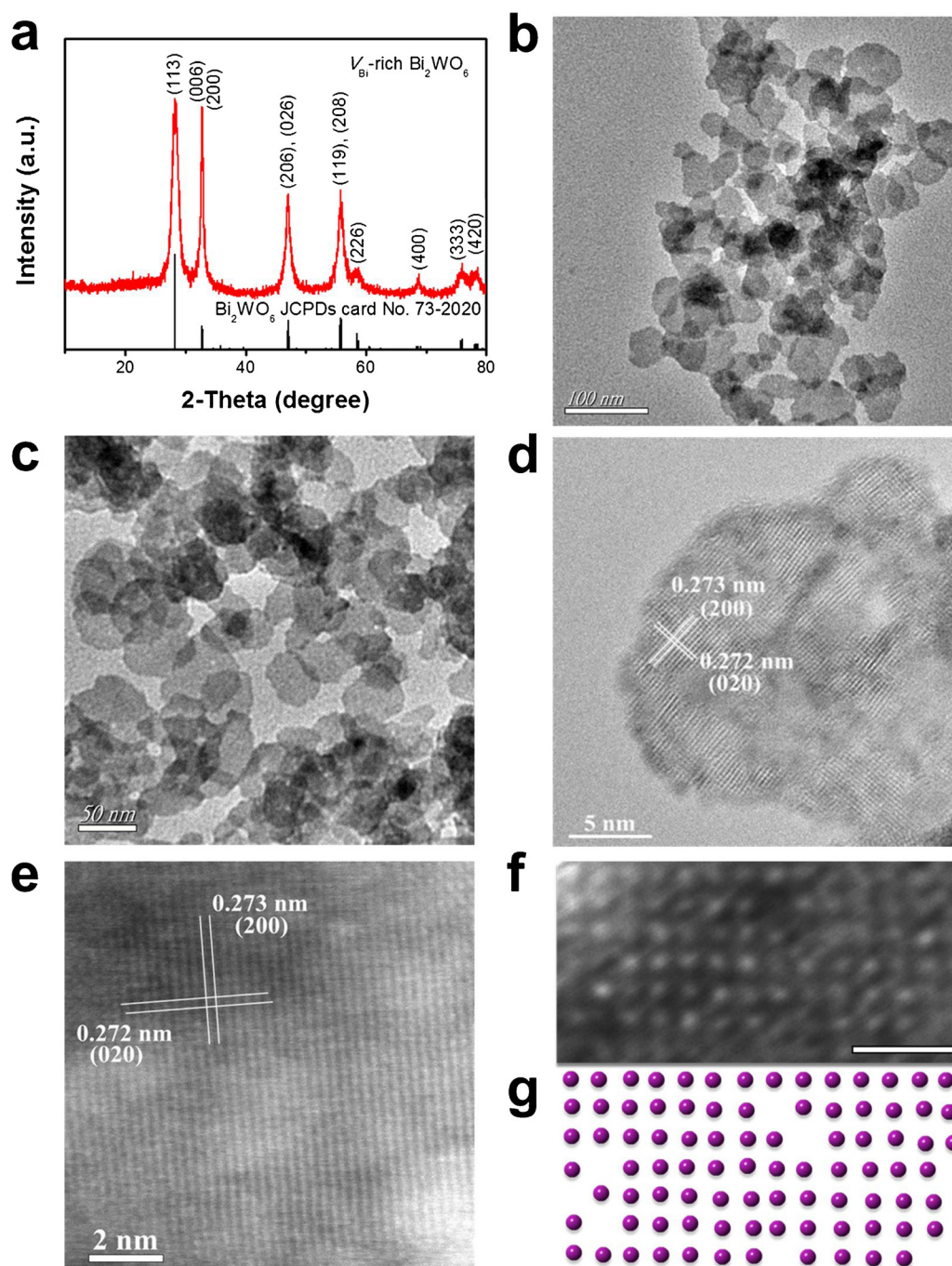


Fig. 1. (a) XRD, (b, c) TEM images, (d) HRTEM image and (e, f) aberration-corrected HAADF-STEM images of the obtained V_{Bi} -rich Bi_2WO_6 , scale bar, 1 nm in f. (g) structural model to show surface Bi vacancies in f, purple balls indicate atomic columns and surface Bi vacancy was indicated as blank in the model. (For interpretation of the references to color in this figure legend, the reader is referred to the web version of this article).

thickness with an average thickness of about 1.4 nm, which was very close to that of single unit cell Bi_2WO_6 slab. Therefore, all of the above results demonstrated the formation of Bi_2WO_6 ultrathin nanosheets with atomically thickness. To disclose the atomic structure of the Bi_2WO_6 ultrathin nanosheets, aberration-corrected scanning transmission electron microscopy using the high-angle annular dark field imaging technique (STEM-HAADF) was directly utilized. The lattice spacing of Bi_2WO_6 was also determined to be 0.273 and 0.272 nm, in good agreement with the HRTEM result (Fig. 1e). Since the $[\text{Bi}_2\text{O}_2]$ layers are exposed outside while the $[\text{WO}_4]$ layers are buried inside in Bi_2WO_6 materials, which means that the outside Bi and O atoms should escape from the lattice more easily to form vacancies [11]. The atomic

resolution STEM image (Fig. 1f) and structural models (Fig. 1g) demonstrated that surface bismuth vacancies have been successful engineered into the Bi_2WO_6 ultrathin nanosheets (V_{Bi} -rich Bi_2WO_6). For make a comparison, the bulk Bi_2WO_6 was also prepared and characterized systematically (Figs. S3, S4).

To further determine the possible existed surface oxygen vacancies, the electron paramagnetic resonance (EPR) spectra was performed on the as-prepared V_{Bi} -rich Bi_2WO_6 . As shown in Fig. 2a, no typical signal of oxygen vacancies in which located at $g = 2.001$ can be observed, revealing the main defect type in V_{Bi} -rich Bi_2WO_6 was isolated bismuth vacancies rather than oxygen vacancies [23]. Furthermore, the bismuth vacancies would lead to the formation of dangling O bonds, which

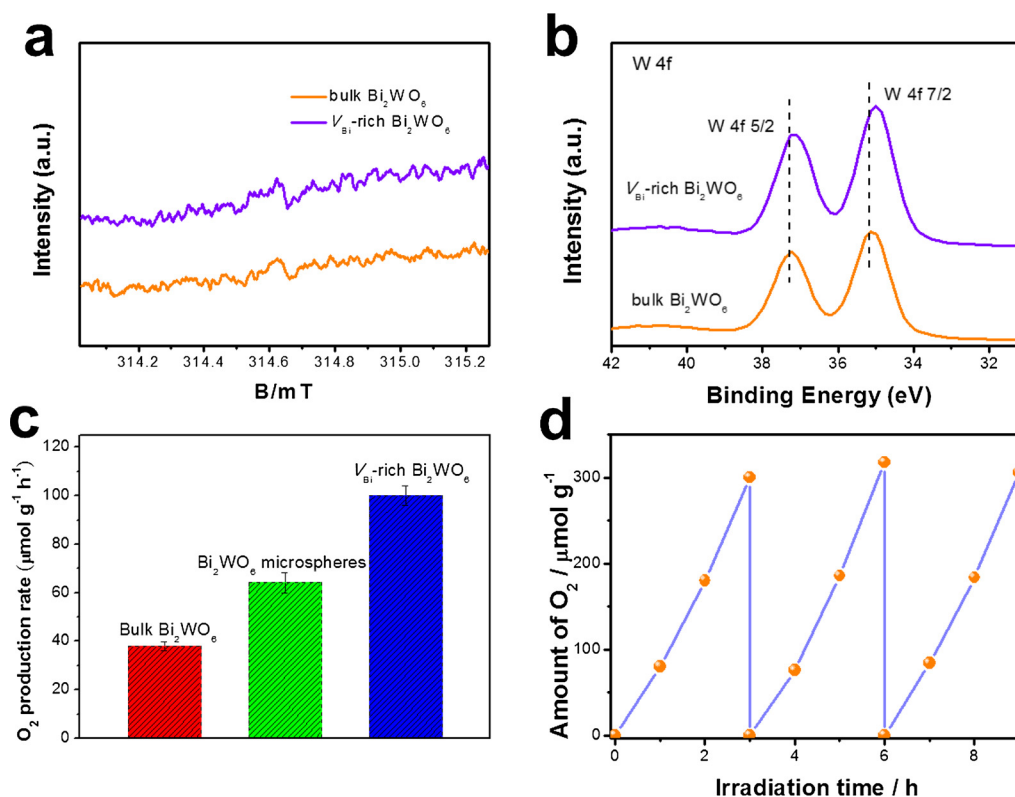


Fig. 2. (a) Electron paramagnetic resonance spectra, (b) the W 4f XPS spectra, (c) photocatalytic oxygen evolution of the V_{Bi} -rich Bi_2WO_6 , Bi_2WO_6 microspheres and bulk Bi_2WO_6 under visible light irradiation, (d) cycling curves of V_{Bi} -rich Bi_2WO_6 .

could accommodate electrons, further testified by the surface charge revealed by zeta-potentials. The V_{Bi} -rich Bi_2WO_6 displayed a zeta potential of -24.2 mV, much increased negative than that of bulk Bi_2WO_6 (-17.1 mV), further suggesting the existence of abundant bismuth vacancies in V_{Bi} -rich Bi_2WO_6 .

To study the surface chemical compositions and valence states of the as-obtained V_{Bi} -rich Bi_2WO_6 , the XPS analysis was carried out. As shown in Fig. S5a, the peaks of Bi, O, W, and C appeared in the XPS survey spectra of the V_{Bi} -rich Bi_2WO_6 sample, revealing the successfully synthesis of Bi_2WO_6 via this ion exchange strategy. The peaks located at 164.1 and 158.8 eV in Fig. S5b can be attributed to the Bi 4f_{5/2} and Bi 4f_{7/2} in $[\text{Bi}_2\text{O}_2]^{2+}$, respectively. From Fig. S5c, the peak centered at 529.9 eV can be ascribed to the oxygen in Bi_2WO_6 crystals. From the high-resolution XPS spectra of W elemental in Fig. 2b, it can be seen that the binding energy of 37.1 and 35.0 eV was corresponding to W 4f_{5/2} and W 4f_{7/2} in the $[\text{WO}_4]^{2-}$, suggesting the existing in a 6+ oxidation state. The slight peak shift to lower binding energy can be found for the V_{Bi} -rich Bi_2WO_6 relative to bulk Bi_2WO_6 , which indicated the variation of the electron density close to the W atoms due to the bismuth vacancies-rich configuration [8]. The Raman analysis (Fig. S6) of V_{Bi} -rich Bi_2WO_6 with peak profile distinction and peak shifting further suggested the significant microstructure difference between V_{Bi} -rich Bi_2WO_6 and bulk Bi_2WO_6 due to the phonon softening and increased electron-phonon coupling in the V_{Bi} -rich Bi_2WO_6 [2].

The photocatalytic activity of the V_{Bi} -rich Bi_2WO_6 was evaluated by water oxidation under visible light irradiation. As shown in Fig. 2c, the bulk Bi_2WO_6 can display an oxygen generation rate for $38.01 \mu\text{mol g}^{-1} \text{h}^{-1}$ under visible light irradiation (300 W Xe arc lamp with a 420 nm cutoff filter), revealing the inherent ability of Bi_2WO_6 for water oxidation. By reducing the thickness to single unit cell and engineering bismuth vacancies, the oxygen generation rate can be improved to $100.13 \mu\text{mol g}^{-1} \text{h}^{-1}$ for the V_{Bi} -rich Bi_2WO_6 , comparable to many oxygen generation photocatalysts (Table S1). For make a comparison, the oxygen generation activity of Bi_2WO_6 microspheres was also

evaluated (the characterizations of Bi_2WO_6 microspheres were shown in Figs. S7, S8). A rate of $64.21 \mu\text{mol g}^{-1} \text{h}^{-1}$ can be achieved for Bi_2WO_6 microspheres [13], which further reveal the advantage of V_{Bi} -rich Bi_2WO_6 . More importantly, the oxygen evolution activity of the recycled V_{Bi} -rich Bi_2WO_6 did not suffer from any significant deterioration after three cycle tests, suggesting the excellent photostability (Fig. 2d).

Generally, three major steps essentially determine the photocatalytic efficiency during the reaction process, namely light absorption, charge separation and migration, as well as interfacial catalytic reactions. To disclose the role of V_{Bi} -rich structure in affecting photocatalysis, a series of characterizations were carried out to study the above-mentioned three aspects. To explore the effect of architectural difference on the light absorption, UV/Vis diffuse reflection spectra (DRS) was carried out on the V_{Bi} -rich Bi_2WO_6 and bulk Bi_2WO_6 . After the thickness of bulk Bi_2WO_6 decreased to single crystal cell, the onset light absorption edge showed obvious blue shift (Fig. 3a). This phenomenon was derived from the well-known quantum confinement effect [24]. It was worth noting that the V_{Bi} -rich Bi_2WO_6 displayed greatly increased light absorption in UV region than that of bulk Bi_2WO_6 , which can be ascribed to that the abundant coordination-unsaturated surface atoms near the bismuth vacancies can better harvesting UV light. The corresponding band gap was calculated to be 2.59 and 2.47 eV for V_{Bi} -rich Bi_2WO_6 and bulk Bi_2WO_6 , respectively (Fig. 3b). To determine the specific surface area of the as-prepared V_{Bi} -rich Bi_2WO_6 , N_2 adsorption-desorption isotherm was conducted (Fig. 3c). Type IV isotherms were observed, suggesting the presence of mesopores formed between Bi_2WO_6 nanosheets. The measured specific surface area was $60.83 \text{ m}^2/\text{g}$ for the V_{Bi} -rich Bi_2WO_6 , approximately 196 times higher than that of bulk Bi_2WO_6 ($0.31 \text{ m}^2/\text{g}$) and also higher than the reported values for Bi_2WO_6 layers [10,11]. The greatly improved specific surface area would in favor of better interfacial contact of water molecule, and subsequent promote the water oxidation processes.

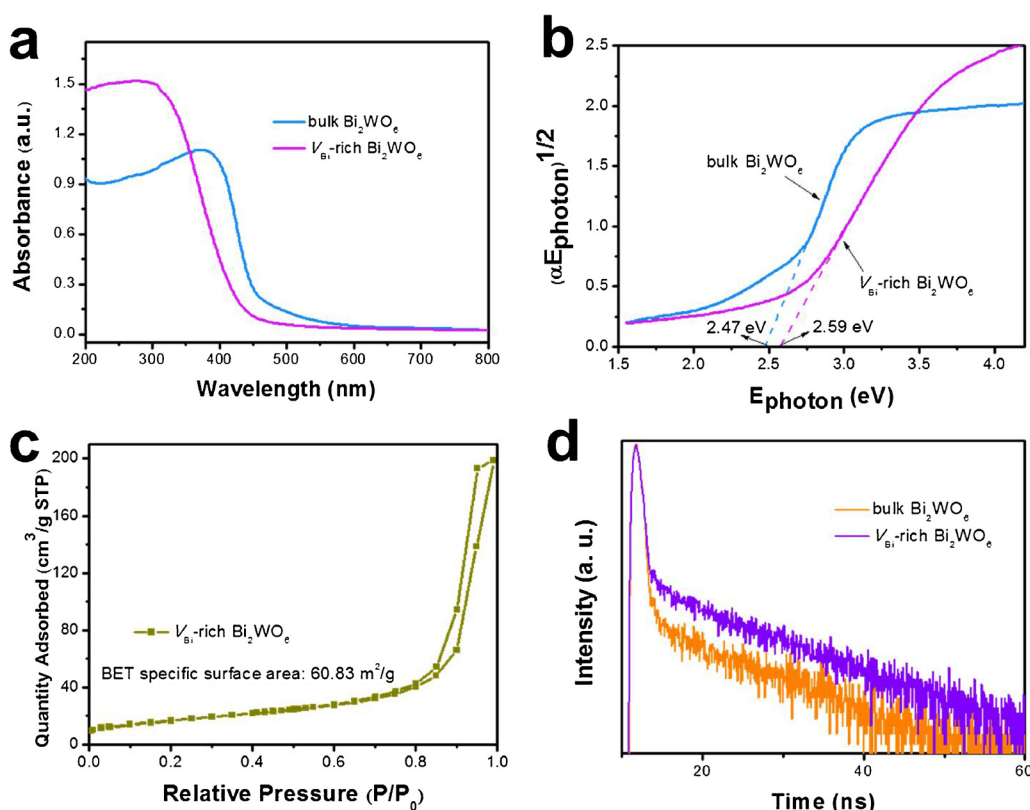


Fig. 3. (a) UV/Vis diffuse reflection spectra and (b) Tauc plot of V_{Bi}-rich Bi₂WO₆ and bulk Bi₂WO₆, (c) Nitrogen adsorption-desorption isotherms of V_{Bi}-rich Bi₂WO₆, (d) time-resolved transient PL decay of V_{Bi}-rich Bi₂WO₆ and bulk Bi₂WO₆. (For interpretation of the references to color in the text, the reader is referred to the web version of this article).

To determine the effect of bismuth vacancies on electronic structure, the density of states (DOS) of V_{Bi}-rich Bi₂WO₆ and bulk Bi₂WO₆ was calculated through density-functional-theory (DFT). To clarify the influence of ultrathin thickness on electronic structure, single unit cell Bi₂WO₆ without defects were also studied. As shown in Fig. 4, the perfect Bi₂WO₆ ultrathin nanosheets showed wider band gap relative to bulk Bi₂WO₆, which is consistent to the DRS analysis. After the bismuth vacancy is engineered, a new defect level in forbidden band and increased DOS at the valence band maximum (VBM) can be observed relative to perfect Bi₂WO₆ ultrathin nanosheets (Fig. 4e). This new defect level and increased DOS will in favor of the electron transition into the conduction band under irradiation, enables a higher carrier concentration and increase the electronic conductivity [17,25]. As a consequence, the electric field in the space charge regions will be increased and then boost charge separation. In order to further determine the charge separation and transfer process, time-resolved transient photoluminescence (PL) decay (Fig. 3d) and transient photocurrent response (Fig. S9) were carried out on V_{Bi}-rich Bi₂WO₆ and bulk Bi₂WO₆. The V_{Bi}-rich Bi₂WO₆ exhibited increased radiative lifetime of the charge carriers and improved photocurrent intensity than bulk Bi₂WO₆, revealing the increased charge separation efficiency for V_{Bi}-rich Bi₂WO₆ [26]. The existed bismuth vacancies resulted in more photoexcited electrons captured by the trap states, while the more long-lived, trapped electrons favors promote the electron-hole pair separation efficiency [27,28].

The V_{Bi}-rich Bi₂WO₆ with single unit cell thickness provide the huge surface area, which is beneficial to the interfacial water oxidation reaction. Moreover, the higher charge separation efficiency of V_{Bi}-rich Bi₂WO₆ enabled the high-efficiency utilization of carrier with more holes reaching at the surface to take part in the water oxidation reaction. Furthermore, it is widely accepted that water oxidation is an interfacial reaction in which the water molecule should be initially adsorbed on the surface and involved in the subsequently activation and oxidation process. In that case, the adsorption energy of water molecule onto the surface of Bi₂WO₆ materials is calculated via DFT. As shown in

Fig. S10, the adsorption energy on the surface of V_{Bi}-rich Bi₂WO₆ is −0.566 eV, which is lower than that of bulk Bi₂WO₆ (−0.253 eV). These results undoubtedly revealing that the H₂O molecules are more favorable adsorbed on the surface of V_{Bi}-rich Bi₂WO₆ and build powerful interaction, which is beneficial to interfacial electrons transfer and is valuable for the H₂O molecules activation. As a result, the oxygen generation rate of V_{Bi}-rich Bi₂WO₆ can be greatly improved.

The water oxidation to produce oxygen was an absolute hole-participating reaction, which directly reflect the behavior of photo-generated holes. Therefore, the potential of valence band (VB) greatly affect the oxidizing ability of generated holes. The XPS VB spectra was employed to determine the VB edge of the as-prepared Bi₂WO₆ samples. As shown in Fig. 5a, the bulk Bi₂WO₆ showed the VB edge at 1.72 eV, while the VB edge of V_{Bi}-rich Bi₂WO₆ up-shifted to 1.52 eV. On the basis of the band gaps obtained from the UV/Vis diffuse reflection spectra, the conduction band (CB) edges can be estimated to be −0.75 and −1.07 eV for bulk Bi₂WO₆ and V_{Bi}-rich Bi₂WO₆, respectively (Fig. 5b). Generally, view from the thermodynamics aspect, the holes generated on the more positive VB position will possess stronger oxidizing ability. The bulk Bi₂WO₆ displayed more positive VB position than that of V_{Bi}-rich Bi₂WO₆ and thus should gain the better water oxidation ability. However, it do not accord with the result of photocatalytic water oxidation experiment. The inherent reason should be that kinetic factor play more important role in this system. The unique defect-rich ultrathin structure enable the V_{Bi}-rich Bi₂WO₆ with higher charge separation efficiency and thus more photogenerated holes can involve in the water oxidation process for V_{Bi}-rich Bi₂WO₆ and achieve the improved photocatalytic water oxidation activity.

From another aspect, the up-shifted CB position of V_{Bi}-rich Bi₂WO₆ will provide more reductive photogenerated electrons, and thus the molecule oxygen can be better activated to produce superoxide radicals (O₂^{•−}). To certify this viewpoint, ESR spin-trap tests with 5,5-dimethyl-1-pyrroline N-oxide (DMPO) were performed (Fig. S11) [29]. The V_{Bi}-rich Bi₂WO₆ displayed improved O₂^{•−} signal intensity than that of bulk Bi₂WO₆, further suggesting the better molecule oxygen activation for

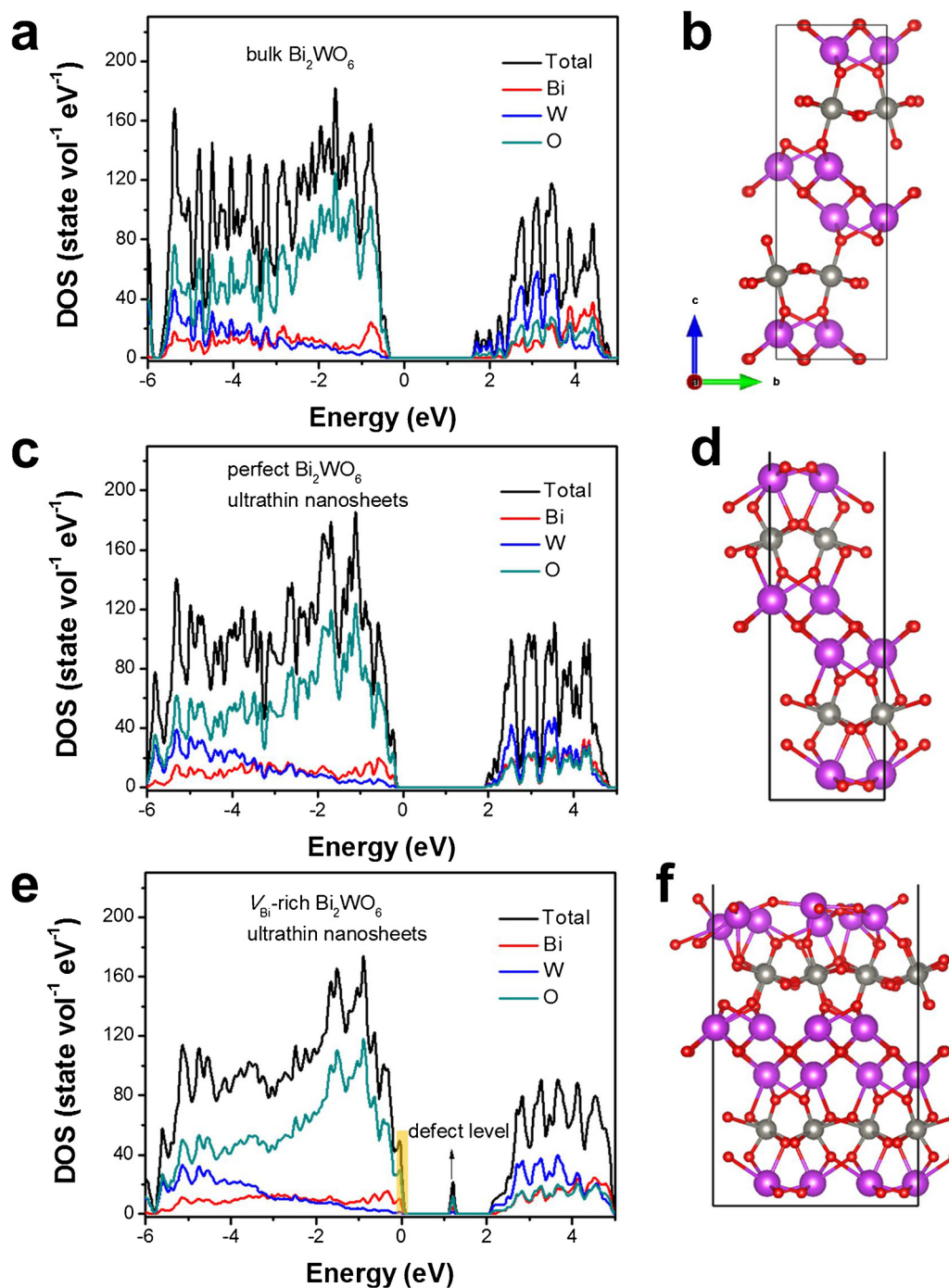


Fig. 4. Calculated density of states of (a) bulk Bi_2WO_6 , (c) perfect Bi_2WO_6 ultrathin nanosheets and (e) V_{Bi} -rich Bi_2WO_6 ultrathin nanosheets; Structure model of (b) bulk Bi_2WO_6 , (d) perfect Bi_2WO_6 ultrathin nanosheets and (f) V_{Bi} -rich Bi_2WO_6 ultrathin nanosheets.

V_{Bi} -rich Bi_2WO_6 . Due to the $\text{O}_2^{\cdot -}$ was an important radicals which can be employed for organic synthesis such as trigger organic aerobic couplings of amines to corresponding imines [30], the generated more $\text{O}_2^{\cdot -}$ enabled V_{Bi} -rich Bi_2WO_6 to be rather promising for photocatalytic organic synthesis.

4. Conclusions

In conclusion, Bi_2WO_6 nanosheets with single unit cell thickness and enriched bismuth vacancies has been controlled prepared. The engineered bismuth vacancies can greatly tune the electronic structure, in which increase the charge density at VBM and build a new defect level

in forbidden band, enabling an effective electron-hole separation. Moreover, the bismuth vacancy structure benefit for the adsorption and activation of water molecule, which favors the oxygen generation catalysis reactions. As a result, the V_{Bi} -rich Bi_2WO_6 showed promoted water oxidation efficiency under visible light irradiation with the oxygen generation rate up to $100.13 \mu\text{mol g}^{-1} \text{h}^{-1}$.

Acknowledgements

This work was financially supported by the National Natural Science Foundation of China (No. 21676128, 21576123, 21476098 and 21471069), Singapore National Research Foundation under NRF RF

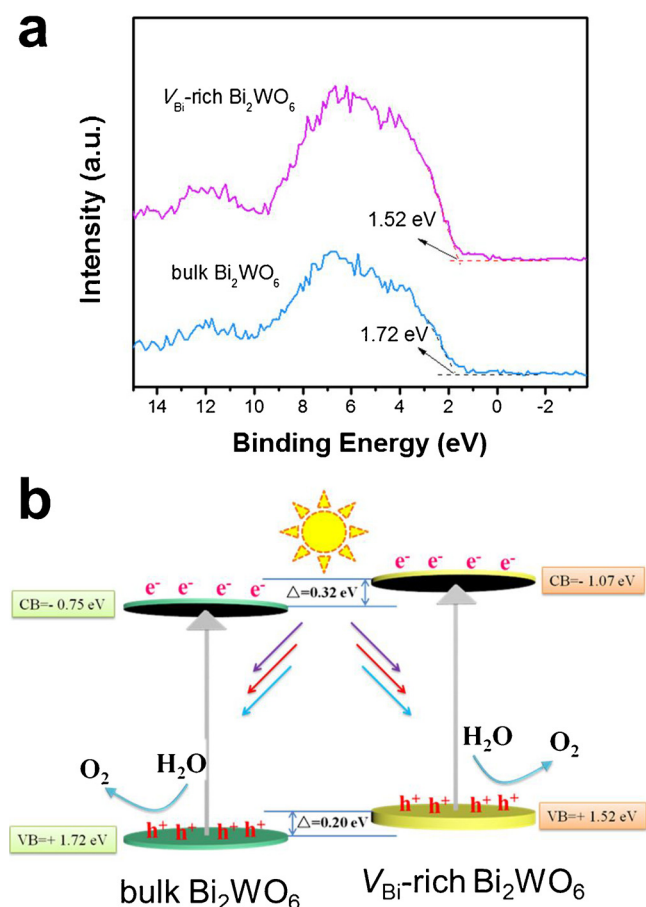


Fig. 5. (a) XPS valence spectra of the obtained samples and (b) schematic band structure of bulk Bi_2WO_6 and V_{Bi} -rich Bi_2WO_6 .

Award No. NRF-RF2013-08, Tier 1 2017-T1-001-075, Academic Research Fund Tier 1 (RG2/16 and RG4/17) and the International Postdoctoral Exchange Fellowship Program of China Postdoctoral Council (No. 20150060).

Appendix A. Supplementary data

Supplementary material related to this article can be found, in the online version, at doi:<https://doi.org/10.1016/j.apcatb.2018.06.066>.

References

- [1] B.C. Qiu, M.Y. Xing, J.L. Zhang, Chem. Soc. Rev. 47 (2018) 2165–2216.
- [2] Y.W. Liu, L. Liang, C. Xiao, X.M. Hua, Z. Li, B.C. Pan, Y. Xie, Adv. Energy Mater. (2016) 1600437.
- [3] G.S. Li, Z.C. Lian, W.C. Wang, D.Q. Zhang, H.X. Li, Nano Energy 19 (2016) 446–454.
- [4] F. Dong, T. Xiong, Y.J. Sun, L.L. Lu, Y.X. Zhang, H.J. Zhang, H.W. Huang, Y. Zhou, Z.B. Wu, Appl. Catal. B 219 (2017) 450–458.
- [5] X.W. Li, W.D. Zhang, W. Cui, Y.J. Sun, G.M. Jiang, Y.X. Zhang, H.W. Huang, F. Dong, Appl. Catal. B 221 (2018) 482–489.
- [6] F.C. Lei, L. Zhang, Y.F. Sun, L. Liang, K.T. Liu, J.Q. Xu, Q. Zhang, B.C. Pan, Y. Luo, Y. Xie, Angew. Chem. Int. Ed. 54 (2015) 9266–9270.
- [7] N. Zhang, R. Ciriminna, M. Pagliaro, Y.J. Xu, Chem. Soc. Rev. 43 (2014) 5276–5287.
- [8] G. Zhang, Z.Y. Hu, M. Sun, Y. Liu, L.M. Liu, H.J. Liu, C.P. Huang, J.H. Qu, J.H. Li, Adv. Funct. Mater. 25 (2015) 3726–3734.
- [9] C.M. Li, G. Chen, J.X. Sun, J.C. Rao, Z.H. Han, Y.D. Hu, Y.S. Zhou, ACS Appl. Mater. Interfaces 7 (2015) 25716–25724.
- [10] Y.G. Zhou, Y.F. Zhang, M.S. Lin, J.L. Long, Z.Z. Zhang, H.X. Lin, J.C.-S. Wu, X.X. Wang, Nat. Commun. 6 (2015) 8340.
- [11] L. Liang, F.C. Lei, S. Gao, Y.F. Sun, X.C. Jiao, J. Wu, S. Qamar, Y. Xie, Angew. Chem. Int. Ed. 54 (2015) 13971–13974.
- [12] S. Murcia-López, K. Villa, T. Andreu, J.R. Morante, ACS Catal. 4 (2014) 3013.
- [13] J. Di, J.X. Xia, Y.P. Ge, H.P. Li, H.Y. Ji, H. Xu, Q. Zhang, H.M. Li, M.N. Li, Appl. Catal. B 168–169 (2015) 51–61.
- [14] H. Wang, W.D. Zhang, X.W. Li, J.Y. Li, W.L. Cen, Q.Y. Li, F. Dong, Appl. Catal. B 225 (2018) 218–227.
- [15] Y.F. Zhao, G.B. Chen, T. Bian, C. Zhou, G.I.N. Waterhouse, L.Z. Wu, C.H. Tung, L.J. Smith, D. O'Hare, T.R. Zhang, Adv. Mater. 27 (2015) 7824–7831.
- [16] J. Di, J.X. Xia, H.M. Li, Z. Liu, Nano Energy 35 (2017) 79–91.
- [17] S. Gao, B.C. Gu, X.C. Jiao, Y.F. Sun, X.L. Zu, F. Yang, W.G. Zhu, C.M. Wang, Z.M. Feng, B.J. Ye, Y. Xie, J. Am. Chem. Soc. 139 (2017) 3438–3445.
- [18] Y.W. Liu, C. Xiao, Z. Li, Y. Xie, Adv. Energy Mater. 6 (2016) 1600436.
- [19] S.B. Wang, L. Pan, J.J. Song, W.B. Mi, J.J. Zou, L. Wang, X.W. Zhang, J. Am. Chem. Soc. 137 (2015) 2975–2983.
- [20] D.F. Yan, Y.X. Li, J. Huo, R. Chen, L.M. Dai, S.Y. Wang, Adv. Mater. 29 (2017) 1606459.
- [21] G. Kresse, J. Furthmüller, Phys. Rev. B 54 (1996) 11169.
- [22] J.P. Perdew, K. Burke, M. Ernzerhof, Phys. Rev. Lett. 77 (1996) 3865.
- [23] H. Li, J. Shang, Z.H. Ai, L.Z. Zhang, J. Am. Chem. Soc. 137 (2015) 6393–6399.
- [24] P. Niu, L.L. Zhang, G. Liu, H.M. Cheng, Adv. Funct. Mater. 22 (2012) 4763–4770.
- [25] F.C. Lei, Y.F. Sun, K.T. Liu, S. Gao, L. Liang, B.C. Pan, Y. Xie, J. Am. Chem. Soc. 136 (2014) 6826–6829.
- [26] Q.H. Zhu, B.C. Qiu, M.M. Du, M.Y. Xing, J.L. Zhang, Ind. Eng. Chem. Res. 57 (2018) 8125–8130.
- [27] X.C. Jiao, Z.W. Chen, X.D. Li, Y.F. Sun, S. Gao, W.S. Yan, C.M. Wang, Q. Zhang, Y. Lin, Y. Luo, Y. Xie, J. Am. Chem. Soc. 139 (2017) 7586–7594.
- [28] J. Di, J. Xiong, H.M. Li, Z. Liu, Adv. Mater. 30 (2018) 1704548.
- [29] J. Di, C. Chen, S.Z. Yang, M.X. Ji, C. Yan, K.Z. Gu, J.X. Xia, H.M. Li, S.Z. Li, Z. Liu, J. Mater. Chem. A 5 (2017) 14144–14151.
- [30] N. Zhang, X.Y. Li, H.C. Ye, S.M. Chen, H.X. Ju, D.B. Liu, Y. Lin, W. Ye, C.M. Wang, Q. Xu, J.F. Zhu, L. Song, J. Jiang, Y.J. Xiong, J. Am. Chem. Soc. 138 (2016) 8928–8935.